RESEARCH ARTICLE | JANUARY 24 2024

Exploring phase formation and magnetic transitions in $Sm(Fe_{1-x}Mn_x)_{14}B$ by Mössbauer spectroscopy

Shengyu Yang ; Jijun Xue ; Bo Zhang; Peng Wu; Yiwen Dong ; Zhiwei Li ; Fashen Li; Liang Qiao

AIP Advances 14, 015146 (2024)
https://doi.org/10.1063/5.0179884

Exploring phase formation and magnetic transitions in $Sm(Fe_{1-x}Mn_x)_{14}B$ by Mössbauer spectroscopy

Cite as: AIP Advances 14, 015146 (2024); doi: 10.1063/5.0179884
Submitted: 5 October 2023 • Accepted: 7 December 2023 •
Published Online: 24 January 2024

Shengyu Yang,[1,2] Jijun Xue,[1] Bo Zhang,[1] Peng Wu,[1] Yiwen Dong,[1] Zhiwei Li,[1] Fashen Li,[1] and Liang Qiao[1,2,a)]

AFFILIATIONS

[1] Institute of Applied Magnetism, Key Laboratory for Magnetism and Magnetic Materials of Ministry of Education, Lanzhou University, Lanzhou 730000, China
[2] Key Laboratory for Special Function Materials and Structure Design of the Ministry of the Education, Lanzhou University, Lanzhou 730000, China

[a)] **Author to whom correspondence should be addressed:** qiaoliang@lzu.edu.cn

ABSTRACT

The $Sm_2(Fe_{1-x}Mn_x)_{14}B$ ($0 \le x \le 0.3$) rare earth alloy was prepared by a reduction-diffusion method, and a corresponding reduction-diffusion model was established. The crystal structure, microscopic morphology, and magnetic properties were systematically characterized to investigate the effect of Mn doping. The results show that the diffusion of Sm into FeB proceeded with the formation of the $Sm_2Fe_{14}B$ phase from the very beginning of the reaction. $Sm_2(Fe_{1-x}Mn_x)_{14}B$ alloy undergoes a transition from the ferromagnetic phase (x = 0) to the paramagnetic phase (x = 0.2), and the average magnetic moment of Fe decreases from 2.066 to 0.719 μ_B as observed by ^{57}Fe Mössbauer spectroscopy. In addition, the Curie temperature decreases rapidly from 620 to 230 K. In other words, a wide temperature-regulation of T_C can be achieved by adjusting the Mn content, which is attributed to the fact that Mn doping greatly weakens the atomic exchange interactions. These results provide value for potential applications of Re–Fe-based alloys in room temperature magnetic refrigeration.

I. INTRODUCTION

Intermetallic compounds containing samarium (Sm) and iron (Fe) have attracted much attention due to their huge magnetostriction. Specifically, the binary compound Sm_2Fe_{17} and the metastable phase $SmFe_7$ exhibit a planar magnetic anisotropy,[1–6] which can be transformed into uniaxial magnetic anisotropy by introducing carbon or nitrogen into the interstitial positions of the crystal lattice. Since the Sm–Fe system appears to be interesting from the viewpoint of finding new high-performance hard or soft magnetic materials, it is important to do more research on the various kinds of systems. For $Sm_2Fe_{14}B$ alloy, it exhibits strong planar anisotropy and outstanding magnetostrictive properties, it has drawn the attention of numerous theoretical and experimental researchers.[7–15] Consequently, various fabrication methods, including magnetron sputtering, melt-spinning and so on, have been employed for the investigation of Sm–Fe–B alloys.

In this work, the $Sm_2(Fe_{1-x}Mn_x)_{14}B$ alloy was prepared using a low-cost reduction-diffusion (R/D) method. We investigated the phase formation behavior through XRD and SEM analyses, and established a corresponding R/D model. The single-phase diffusive motion of rare earth atoms during diffusion reactions is demonstrated. We utilized VSM, ^{57}Fe Mössbauer spectroscopy, and density functional theory calculations to investigate the structural and magnetic properties of $Sm_2(Fe_{1-x}Mn_x)_{14}B$ series with different Mn concentrations. The preferential occupancy information of Mn atoms was obtained through calculations. At x = 0.2, a coexistence of ferromagnetic and paramagnetic phases was observed in the room temperature ^{57}Fe Mössbauer spectrum, accompanied by a significant increase in magnetic entropy. This not only enhances our understanding of the physical properties of (Sm–Fe)-series compounds but also provides new insights into the cause of the increase in magnetic entropy in magnetothermic materials.

II. EXPERIMENTS

Mn-doped $Sm_2(Fe_{1-x}Mn_x)_{14}B$ alloys ($0 \le x \le 0.3$) were prepared using a reduction-diffusion method. The raw materials Sm_2O_3, MnO_2, Fe, FeB, and Ca were thoroughly mixed using mechanical stirring in a vacuum environment. The reduction process was carried out at 1120 K, followed by a diffusion process at 1420 K, resulting in the formation of $Sm_2(Fe_{1-x}Mn_x)_{14}B$ alloys. Subsequently, it was ball-milled and washed to remove calcium. The remaining CaO and unreacted Ca were removed using a 5% ammonium acetate solution.

The phase constitution of the sample was identified using a PANalytical X'Pert Pro diffractometer (conditions: Cu Ka radiation, 40 kV and 40 mA, 2⊖ range 10–90°, and step 0.016). The microstructures and chemical compositions of the samples were analyzed by a scanning electron microscope (SEM, Apreo S) with energy dispersive x-ray spectroscopy (EDS). The room-temperature hysteresis loops were obtained through a vibrating sample magnetometer (Micro-Sense EV9), which can reach a magnetic field of up to 2 T. The Curie temperature was determined using a custom-designed measurement setup. A permanent magnet was placed at the top of a thermogravimetric analyzer (TGA) to record mass changes, allowing us to obtain the Curie temperature. Transmission Mössbauer spectroscopy studies were performed using a conventional constant acceleration drive with a ^{57}Co source. The absorbers were prepared in powder form (10 mg of natural Fe/cm^2). The velocity calibration was performed with α-Fe at room temperature. The temperature dependence of magnetization was measured using a Physical Property Measurement System (PPMS) from Quantum Design, Inc.

All calculations were performed using the WIEN2k package.[16,17] The full-potential linearized augmented plane-wave (FLAPW) method was adopted, and the generalized gradient approximation (GGA) (Perdew–Burke–Wang form) was employed for the exchange-correlation potential. Throughout the present calculation, we take R_{MT} = 2.45, 2.03, 1.8, 2.1 AU for Sm, Fe, B, Mn ions, respectively. The potential and the charge density in the MT-spheres were expanded in the spherical harmonics with l_{max} = 10.0. The plane-wave cut-off parameter ($R_{mt} \times K_{max}$) was 7.0, and the magnitude of the largest vector G_{max} was 14.0. The energy convergence relative to the number of K points was checked that the above parameters are reliable.

III. RESULTS AND DISCUSSION

Products obtained after different reduction and diffusion times were characterized by x-ray diffraction, as shown in Figs. 1(a) and 1(b). With increasing reduction time, Sm_2O_3 gradually transformed into SmO and Sm_2O, eventually converting to pure Sm, while generating CaO. The iron content remained relatively constant. As the diffusion time increased, the diffraction peak of $Sm_2Fe_{14}B$ gradually intensified, accompanied by a significant decrease in the intensity of the Fe diffraction peak, which completely disappeared at t = 5 h. The major observed diffraction peaks corresponded to $Sm_2Fe_{14}B$ and CaO. This implies the successful formation of the $Sm_2Fe_{14}B$ alloy after 5 h of diffusion, achieving complete diffusion between Sm and FeB. The conversion process of $Sm_2Fe_{14}B$ alloy can be represented by Eqs. (1)–(4). In addition, for the reduction-diffusion process, the control of reduction time and diffusion time is particularly important, which will affect the final product. Less reduction time will lead to the lack of rare earth content during diffusion. Less diffusion time will result in insufficient diffusion, and longer diffusion time will result in volatilization of rare earth elements and failure to obtain the desired phase,

$$Sm_2O_3 + Ca = 2\,SmO + CaO, \quad (1)$$

$$2\,SmO + Ca = Sm_2O + CaO, \quad (2)$$

$$Sm_2O + Ca = 2\,Sm + CaO, \quad (3)$$

$$Sm + Fe + FeB \rightarrow Sm_2Fe_{14}B. \quad (4)$$

The XRD refinements of the x = 0, 0.1, 0.2, and 0.3 obtained at room temperature are presented in Fig. 1(c). Table I gives the lattice parameters and the steadiness indices for the refinement outcomes. It can be seen that $Sm_2Fe_{14}B$ alloys crystallizes in the tetragonal $Nd_2Fe_{14}B$-type structure. When Fe is substituted by Mn to x = 0.3, the tetragonal $Nd_2Fe_{14}B$-type structure of major phase is not changed. As shown in Fig. 1(d), the lattice parameters a, c and unit cell volume increase with increasing Mn substitution amount, which is attributed to the atomic radius of Mn being larger than Fe.

To investigate the formation process of the $Sm_2Fe_{14}B$ alloy, SEM images of the reduction-diffusion products at different diffusion times (0, 1, 2, 4, and 5 h) were obtained, as shown in Figs. 2(a)–2(e). The dark gray, gray, and black areas in each image represent the Fe phase, $Sm_2Fe_{14}B$ phase, and CaO phase, respectively. Researchers observed that the diffusion process of rare-earth metal toward transition metal is a unidirectional reaction process.[5,18] The elemental mapping images of $Sm_2Fe_{14}B$ after four hours of diffusion are presented in Figs. 2(f)–2(i). The single-phase diffusion of elemental Sm into FeB can be demonstrated in terms of brightness and darkness. As the diffusion time increases, the radius of the Fe core gradually reduces, shrinking to merely 1–2 μm after four hours of diffusion.

As the diffusion of Sm and FeB to form the Sm–Fe–B alloy is a progressive process from outside to inside, an unreacted shrinking core model with spherical particles is used to illustrate the entire R/D reaction. Table II lists the thicknesses of the $Sm_2Fe_{14}B$ compound layer at different reaction times. Here, D_0 represents the initial radius of the iron particle, D signifies the radius of the iron core at reaction time t, and $(D_0 - D)$ denotes the layer thickness of the $Sm_2Fe_{14}B$ alloy. Based on Table II, the square of the thickness of the $Sm_2Fe_{14}B$ alloy layer $[(D_0 - D)^2]$ is plotted against reaction time t as depicted in Fig. 3. Thus, the relationship between the thickness of the alloy layer and reaction time can be expressed by

$$(D_0 - D)^2 = 89.97\,t. \quad (5)$$

Therefore, assuming that the particle is an ideal sphere ball, the complete reaction time for 20 μm iron powder particles is 4.45 h. In the experiment, the diffusion of the 20 μm Fe powder was completed in 5 h, which is consistent with the calculation results of the model. This model has certain guiding significance for Fe with different

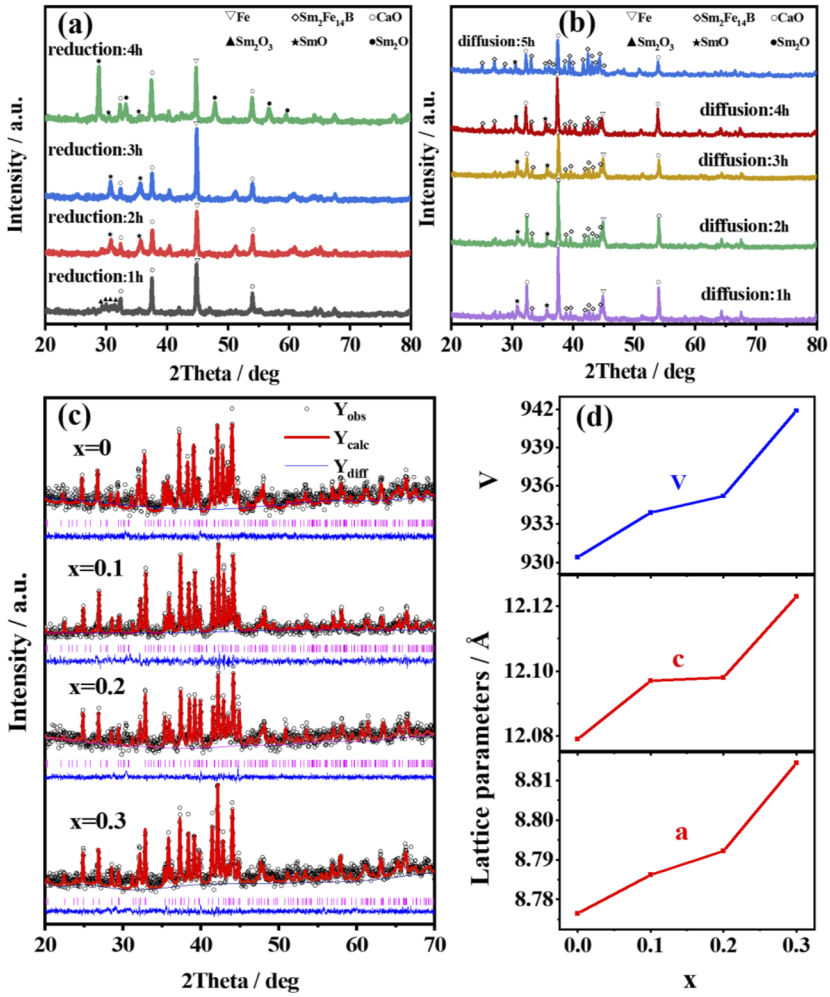

FIG. 1. (a) XRD patterns of the sample after 1, 2, 3, and 4 h of reduction at 1120 K. (b) XRD patterns of the sample after 1, 2, 3, 4, and 5 h of diffusion at 1420 K. (c) The XRD patterns and their refinements of $Sm_2(Fe_{1-x}Mn_x)_{14}B$ ($0 \le x \le 0.3$) alloys along with their lattice parameters and cell volume (d) a, c, and V.

TABLE I. Refined structural parameters of XRD patterns of $Sm_2(Fe_{1-x}Mn_x)_{14}B$.

Parameters	x = 0	x = 0.1	x = 0.2	x = 0.3
a (Å)	8.7765(5)	8.7862(7)	8.7922(8)	8.8144(9)
c (Å)	12.0793(9)	12.097(1)	12.098(1)	12.123(1)
V (Å^3)	930.4(1)	933.9(2)	935.2(2)	941.9(3)
R_{wp}	3.0%	5.0%	3.39%	3.82%

particle sizes as raw materials for reduction diffusion processes. All samples in this experiment were prepared using this model as a reference.

The preferred position of Mn in $Sm_2Fe_{14}B$ was determined by first-principles density functional calculations. This serves as the foundation for subsequent fitting of the ^{57}Fe Mössbauer spectra of doped samples. The substitution energy of Mn in $Sm_2(Fe, Mn)_{14}B$, i.e., the change in the formation energy of Mn-substituted $Sm_2(Fe, Mn)_{14}B$ with respect to $Sm_2Fe_{14}B$ is[19]

$$E_{sub} = E_{Sm_2(Fe_{1-x}Mn_x)_{14}B} - E_{Sm_2Fe_{14}B} - E_{Mn} + E_{Fe}. \quad (6)$$

$E_{Sm2(Fe1-xMnx)_{14}B}$ and $E_{Sm2Fe_{14}B}$ are the total energy per unit cell in the ground state, respectively. E_{Fe} and E_{Mn} are the total energies per atom in the ground state for metallic Mn and Fe, respectively.

The total energy calculations indicate that the substitution energy of Fe by Mn varies significantly at the different Fe sites (see Table III). With the exception of the 4e site, the substitution energy of Mn at other sites is positive, indicating an unfavorable scenario for the substitution of Mn. However, at the 4e site, the substitution energy for Mn is negative (−0.7824 eV), suggesting a favorable condition for Mn substitution. In other words, Mn tends to occupy preferentially the sites of 4e site, followed by $8j_2$ and $16k_1$ sites, while avoiding the 4c, $8j_1$, and $16k_2$ sites.

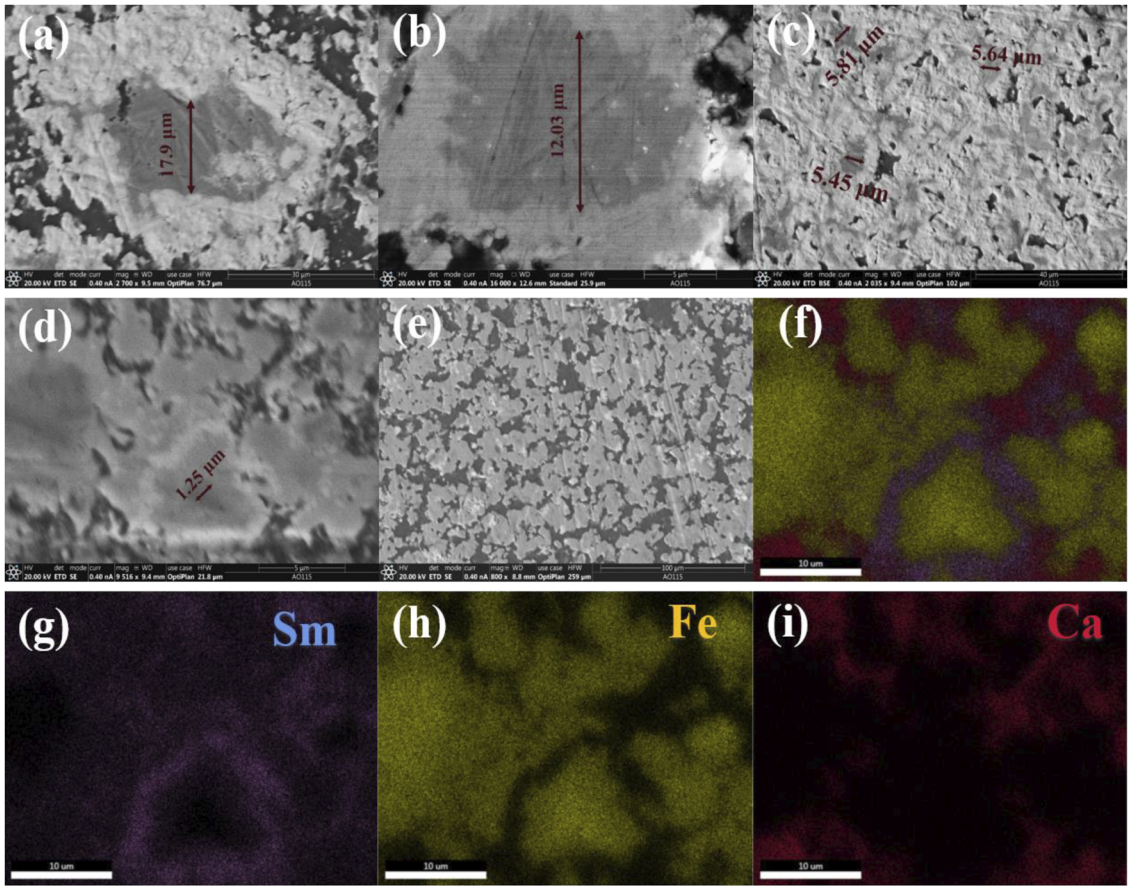

FIG. 2. SEM photographs of $Sm_2Fe_{14}B$ alloys for different reaction times: (a) 0 h, (b) 1 h, (c) 2 h, (d) 4 h, and (e) 5 h. The corresponding elemental mapping images of $Sm_2Fe_{14}B$ after diffusion for 4 h (f)–(i).

TABLE II. Thickness of $Sm_2Fe_{14}B$ alloy layer for different reaction times.

Reaction time (t/h)	0	1	2	4
$(D_0 - D)$ (μm)	2.1	7.97	14.37	18.75
$(D_0 - D)^2$ (μm^2)	4.41	63.52	206.5	351.56

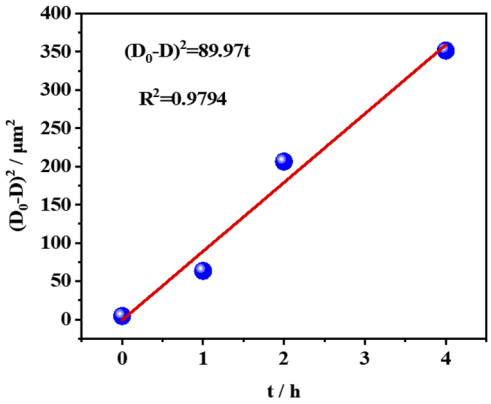

FIG. 3. Plot of $(D_0 - D)^2$ vs reaction time.

Based on the results of the first principle density functional calculations, Mn predominantly occupies the 4e and $8j_2$ sites, followed by the 4c and $16k_1$ sites. On this basis, the Mössbauer spectra of Mn-doped samples were fitted. The fitting results are self-consistent and are shown in Fig. 4. The hyperfine parameters and near-neighbor atomic environments of different Fe sites for $Sm_2(Fe_{1-x}Mn_x)_{14}B$ (x = 0, 0.2) are listed in Table IV. The spectra evolve from the original symmetric six-line peak (x = 0) to a double peak (x = 0.3) with increasing Mn concentration, indicating that the sample undergoes a magnetic transition process from a ferromagnetic phase to a paramagnetic phase. The precursor (x = 0) is fitted with six sets of six-line sub-spectra, corresponding to six nonequivalent Fe sites in the 2:14:1 tetragonal phase. In addition, the relaxation frequency of the small particle size is higher than the Larmor frequency of the ^{57}Fe nucleus, causing these particles to produce a double-peaked signal in the Mössbauer spectrum.[20] For the 2:14:1 phase, generally, the major contribution to the hyperfine field is the Fermi contact

TABLE III. The substitution energy E_{sub} (eV/atom) for the different Fe sites in $Sm_2(Fe, Mn)_{14}B$.

Site	$16k_1$	$16k_2$	$8j_1$	$8j_2$	4c	4e
E_{sub} (eV/atom)	0.2334	0.2838	0.2726	0.2325	0.2402	−0.7824

term, whose transferred field from the iron near-neighbors depends upon their number.[21] Since B atoms behave as electron donors to Fe atoms according to the crystalline electric field effects, B atoms are considered to be able to reduce B_{hf} of near Fe atoms.[21–24] The number and distance between Fe and its nearest B neighbors, as well as the size of the Wigner–Seitz volume, were further investigated.[23] It can be concluded that the maximum of B_{hf} occurs at the $8j_2$ site because it has the largest Fe coordination as well as the largest Wigner–Seitz volume. The second largest B_{hf} occurs at the $16k_2$ site as the distance of $16k_2$ − B is far greater than that of $16k_1$ − B, and following that is the $16k_1$ position. By extension, the order of the hyperfine fields can be determined as follows: $B_{hf}(8j_2) > B_{hf}(16k_2) > B_{hf}(16k_1) > B_{hf}(4e) > B_{hf}(8j_1) > B_{hf}(4c)$. In $Sm_2(Fe_{0.9}Mn_{0.1})_{14}B$, the Fe at sites 4e and $8j_2$ has been mostly replaced. The four inequivalent Fe sites in the 2:14:1 phase is mainly 4c, $8j_1$, $16k_1$, and $16k_2$. The B_{hf} at four Fe sites takes the order of $B_{hf}(8j_1) > B_{hf}(4c) > B_{hf}(16k_2) > B_{hf}(16k_1)$. The substitution of Fe atoms by Mn at the 4e and $8j_2$ positions has an impact on the environment of other sites, thereby leading to changes in the hyperfine fields. As the Mn content increases further to 0.2, it can be observed that both six-line and doublet spectra are present in the sub-spectrum. This indicates the coexistence of ferromagnetic and paramagnetic phases in the alloy and that the ferromagnetic phase occupies only 20.3%. In other words, the Curie temperature of $Sm_2(Fe_{0.8}Mn_{0.2})_{14}B$ is located near room temperature. When x reaches 0.3, only two doublet spectra can be observed in the sub-spectrum, indicating that the alloy has completely transitioned into a paramagnetic state at room temperature. For the $Sm_2(Fe_{1-x}Mn_x)_{14}B$ alloys with x values of 0, 0.1, and 0.2, the average Fe magnetic moments at each site were determined as 2.066, 1.233, and 0.719 μ_B, respectively, using a conversion factor of

TABLE IV. Hyperfine parameters of the x = 0 and the x = 0.2 at room temperature. The IS is relative to the α-Fe.

	IS	QS	B_{hf}	Phase	Atomic environment
x = 0	−0.0537	−0.1532	27.2735	4c	8Fe, 4Sm, 0B
	−0.1593	0.4004	29.9074	4e	9Fe, 2Sm, 2B
	−0.4113	−0.2726	27.8575	$8j_1$	9Fe, 3Sm, 0B
	0.0014	0.4378	35.1641	$8j_2$	12Fe, 2Sm, 0B
	−0.1764	−0.6273	30.9767	$16k_1$	10Fe, 2Sm, 1B
	−0.1655	0.0097	31.6887	$16k_2$	10Fe, 2Sm, 0B

	IS	QS	B_{hf}	Phase	Atomic ratio (%)
x = 0.2	0.0491	0.0635	9.6583	$8j_1$	12.9
	0.0493	−0.0353	12.7836	$16k_2$	7.4
	−0.095 57	−0.2043	<4	Ferromagnetic phase	32.6
	−0.0017	0.7809		Paramagnetic phase	47.1

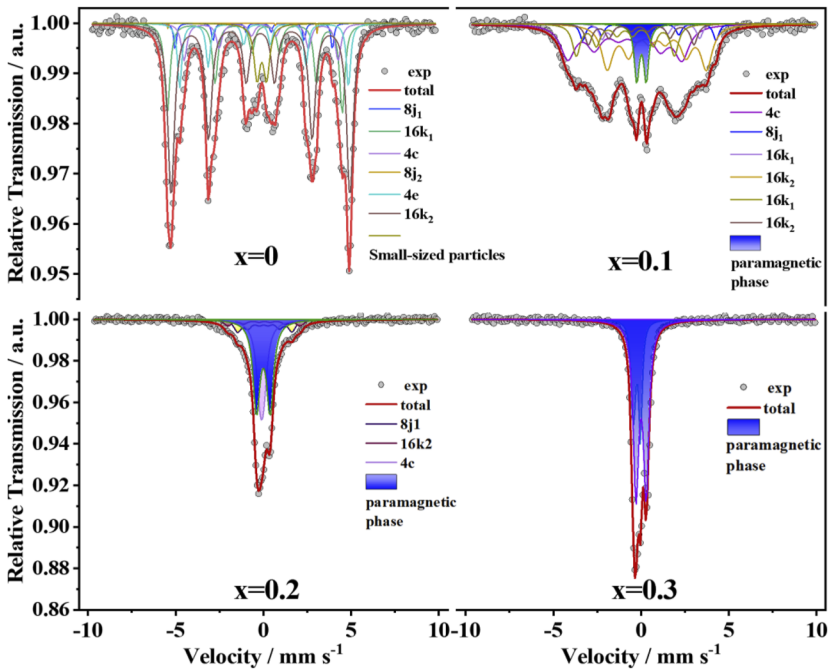

FIG. 4. Mössbauer spectra for $Sm_2(Fe_{1-x}Mn_x)_{14}B$ alloys with different Mn content at room temperature.

15 T/μ_B.[21,25] This is a consequence of the increase in the content of the paramagnetic phase (blue shaded area).

The Curie temperatures of $Sm_2(Fe_{1-x}Mn_x)_{14}B$ ($0 \le x \le 0.3$) alloys were measured as shown in Fig. 5(a). With the increase in x, the Curie temperature decreases from 620 to 230 K. When x = 0.2, the Curie temperature decreases to 300 K, which is near room temperature, which is consistent with the conclusion drawn by the Mössbauer spectrum. The magnetization curves of this sample were measured at different temperatures [see Fig. 5(c)] and the magnetic entropy was calculated by Eq. (7).[26] The maximum value of magnetic entropy is close to room temperature. This indicates that the sample can be used as a potential room temperature magnetic refrigeration material. Figure 5(d) is Arrott plots of $Sm_2(Fe_{1-x}Mn_x)_{14}B$ alloys. It can be clearly seen that the experimental point near T_C shows a straight line with positive slope instead of an S-shaped curve.[27–29] This indicates that the process belongs to the secondary phase transition, in this case a magnetic phase transition. The hysteresis loops of $Sm_2(Fe_{1-x}Mn_x)_{14}B$ alloys were measured at 300 K [see Fig. 5(b)], with saturation magnetization values of 23.3234, 13.3339, 5.3064, and 0.3057 μ_B/f.u., respectively. There is a significant decrease in saturation magnetization intensity at room temperature due to a rapid decrease in Curie temperature. According to Belorizky's viewpoint,[30] In the $Re_2Fe_{14}B$ series materials, T_C is directly related to the exchange interaction between atoms [see Eq. (8)]. The exchange interaction between iron atoms (Fe–Fe coupling) is stronger than the one between iron and rare-earth (R–Fe coupling) sublattices, as well as the exchange interaction within the rare-earth (R–R coupling) sublattice,

$$\Delta S_M = (T,H) = S_M(T,H) - S_M(T,0) = \int_0^H \left(\frac{\partial M}{\partial T}\right)_H dH, \quad (7)$$

$$T_C = \frac{1}{2}(\Theta_0 + \Theta_R) + \frac{1}{2}\sqrt{(\Theta_0 + \Theta_R)^2 + 4(\Theta_{RFe}^2 - \Theta_0\Theta_R)}, \quad (8)$$

where Θ_0 represents the exchange interaction between iron atoms, Θ_R represents the exchange interaction between iron and rare-earth, and Θ_{RFe} represents the exchange interaction between rare-earth and rare-earth.

A major change in magnetism can be attributed to the interaction coupling of magnetic particles. In Re–Fe–based compounds, it is predominantly determined by Fe–Fe interactions.[30] When Mn substitutes for Fe in $Sm_2Fe_{14}B$, partial Fe–Fe interactions are replaced by Mn–Mn or Fe–Mn interactions,[6] thereby weakening the ferromagnetic interactions between Fe atoms, resulting in a significant decrease in the Curie temperature. Therefore, we have achieved a wide-range modulation of the Curie temperature by altering the interatomic exchange interactions.

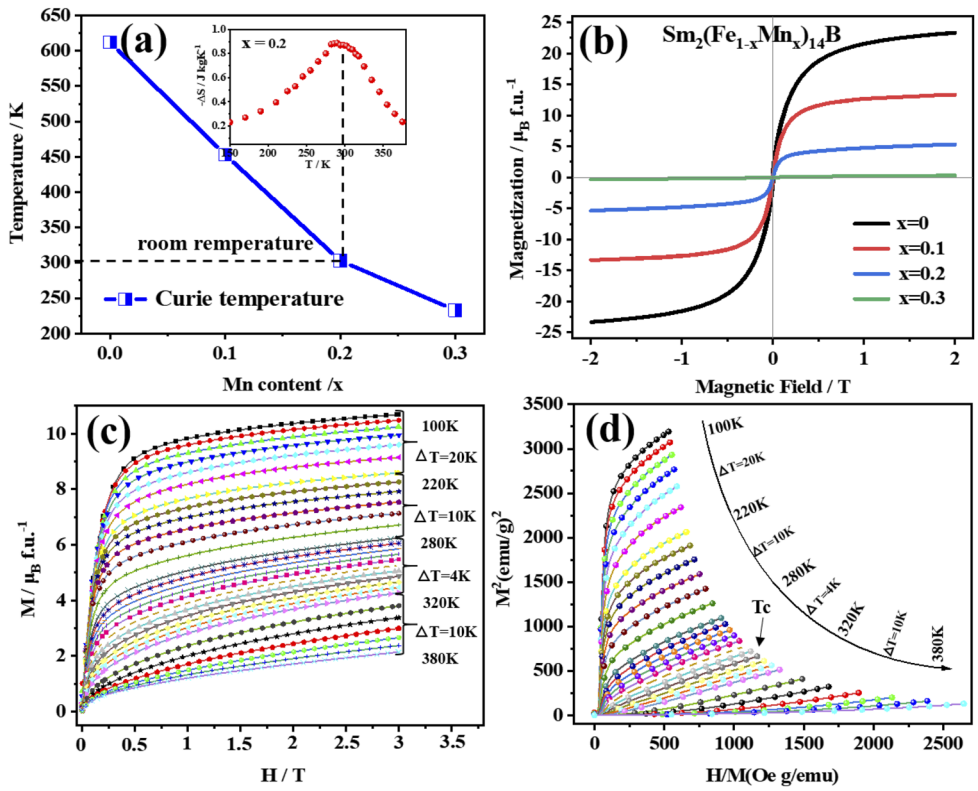

FIG. 5. Curie temperature (a) and magnetic hysteresis loops (b) of $Sm_2(Fe_{1-x}Mn_x)_{14}B$ ($0 \le x \le 0.3$) alloys. Magnetization isotherms (c) and Arrott plots (d) of $Sm_2(Fe_{0.8}Mn_{0.2})_{14}B$.

IV. CONCLUSIONS

In this study, a series of $Sm_2(Fe_{1-x}Mn_x)_{14}B$ ($0 \le x \le 0.3$) samples were synthesized by the reduction-diffusion method. Based on the studies of structural and magnetic properties, the main conclusion is presented as follows:

(1) Based on kinetic analysis, we concluded that the relationship between the thickness of the $Sm_2Fe_{14}B$ alloy layer growing on the iron crystal surface and the reaction time conforms to the parabolic law. The growth model is defined as $(D_0 - D)^2 = 89.97$ t. This offers valuable guidance for the production of samples using the reduction-diffusion process.
(2) For the Mn occupation, based on density functional theory calculations, it is determined that Mn atoms preferentially occupy the 4e, $8j_2$, and $16k_1$ sites of Fe while avoiding the 4c, $8j_1$, and $16k_2$ sites.
(3) For the Mössbauer spectrum, the spectral line changes from a six-line peak to a double peak, realizing a magnetic transition. Correspondingly, the Curie temperature of $Sm_2(Fe_{0.8}Mn_{0.2})_{14}B$ decreases from 620 to 230 K, which is attributed to the doping of Mn atoms significantly weakening the interatomic exchange interactions. Furthermore, a significant increase in magnetic entropy is observed in $Sm_2(Fe_{0.8}Mn_{0.2})_{14}B$ at room temperature. This provides new insights into the application of rare-earth iron-based materials in room-temperature magnetic refrigeration.

Collectively, our work provides a comprehensive understanding of the inner relationships among site occupation and magnetic properties of $Sm_2(Fe_{1-x}Mn_x)_{14}B$. This will soon drive the application of rare-earth alloys in room-temperature magnetic refrigeration.

ACKNOWLEDGMENTS

Project supported by the National Key Research and Development Program of China (Grant No. 2021YFB3501302), the National Natural Science Foundation of China (Grant No. 51731001), and the Fund from the State Key Laboratory of Baiyunobo Rare Earth Resource Researches and Comprehensive Utilization's Key Research and Development Projects. This work was supported by the Supercomputing Center of Lanzhou University.[31]

AUTHOR DECLARATIONS

Conflict of Interestc

The authors have no conflicts to disclose.

Author Contributions

Shengyu Yang: Writing – original draft (equal); Writing – review & editing (equal). **Jijun Xue**: Data curation (equal). **Bo Zhang**: Formal analysis (equal). **Peng Wu**: Supervision (equal). **Yiwen Dong**: Formal analysis (equal). **Zhiwei Li**: Supervision (equal). **Fashen Li**: Supervision (equal). **Liang Qiao**: Writing – review & editing (equal).

DATA AVAILABILITY

The data that support the findings of this study are available from the corresponding author upon reasonable request.

REFERENCES

[1]L. Bessais, C. Djéga-Mariadassou, H. Lassri, and N. Mliki, "Nanocrystalline metastable 2/17 and 1/12 precursors: A promising class of hard magnetic materials," J. Appl. Phys. **106**(10), 103904 (2009).
[2]Y. Harashima, T. Fukazawa, H. Kino, and T. Miyake, "Effect of *R*-site substitution and the pressure on stability of RFe_{12}: A first-principles study," J. Appl. Phys. **124**(16), 163902 (2018).
[3]A. Ludwig and E. Quandt, "Giant magnetostrictive thin films for applications in microelectromechanical systems (invited)," J. Appl. Phys. **87**(9), 4691–4695 (2000).
[4]D.-N. Nguyen and H.-C. Dam, "Machine learning-aided Genetic algorithm in investigating the structure–property relationship of $SmFe_{12}$-based structures," J. Appl. Phys. **133**(6), 133 (2023).
[5]S. Okada and K. Takagi, "Novel synthesis of single-crystalline $TbCu_7$-type Sm–Fe powder by low-temperature reduction-diffusion process using molten salt," J. Rare Earths **40**(7), 1126–1133 (2022).
[6]Y. Wang, W. J. Ren, Z. H. Wang, Y. Q. Zhang, J. Li, and Z. D. Zhang, "Effect of Mn substitution for Fe on magnetic and magnetostrictive properties of $SmFe_2$ compound," J. Appl. Phys. **111**(7), 07A901 (2012).
[7]C. F. Xu, K. H. Chen, Z. F. Gu, D. D. Ma, L. Y. Cheng, G. Cheng, and G. H. Rao, "Experimental determination of the phase relations of the Sm–Fe–B ternary system at 973 K," J. Alloys Compd. **667**, 240–247 (2016).
[8]R. J. Radwański and J. J. M. Franse, "Rare-earth contribution to the magnetocrystalline anisotropy energy in $R_2Fe_{14}B$," Phys. Rev. B **36**(16), 8616–8621 (1987).
[9]F. Maruyama and H. Nagai, "Magnetic properties of Sm–Fe–B compounds," J. Alloys Compd. **393**(1–2), 61–65 (2005).
[10]Z. W. Liu, Y. Liu, P. K. Deheri, R. V. Ramanujan, and H. A. Davies, "Improving permanent magnetic properties of rapidly solidified nanophase RE–TM–B alloys by compositional modification," J. Magn. Magn. Mater. **321**(15), 2290–2295 (2009).
[11]S. Hirosawa, Y. Matsuura, H. Yamamoto, S. Fujimura, M. Sagawa, and H. Yamauchi, "Magnetization and magnetic anisotropy of $R_2Fe_{14}B$ measured on single crystals," J. Appl. Phys. **59**(3), 873–879 (1986).
[12]E. B. Boltich, E. Oswald, M. Q. Huang, S. Hirosawa, W. E. Wallace, and E. Burzo, "Magnetic characteristics of $R_2Fe_{14}B$ systems prepared with high purity rare earths (R = Ce, Pr, Dy, and Er)," J. Appl. Phys. **57**, 4106–4108 (1985).
[13]T. Shima, H. Yokoyama, and H. Fujimori, "Magnetostriction and magnetic properties of Sm–Fe–B and Tb–Fe–B thin films and multilayers," J. Alloys Compd. **258**(1–2), 149–154 (1997).
[14]S. H. Lim, Y. S. Choi, S. H. Han, H. J. Kim, T. Shima, and H. Fujimori, "Magnetostriction of Sm–Fe and Sm–Fe–B thin films fabricated by RF magnetron sputtering," J. Magn. Magn. Mater. **189**(1), 1–7 (1998).
[15]J. M. Le Breton and O. Crisan, "A Mössbauer investigation of amorphous Sm–Fe–B ribbons under applied field," J. Alloys Compd. **351**(1–2), 59–64 (2003).
[16]K. Schwarz, P. Blaha, and G. K. H. Madsen, "Electronic structure calculations of solids using the WIEN2k package for material sciences," Comput. Phys. Commun. **147**(1–2), 71–76 (2002).
[17]G. K. H. Madsen, P. Blaha, K. Schwarz, E. Sjöstedt, and L. Nordström, "Efficient linearization of the augmented plane-wave method," Phys. Rev. B **64**(19), 195134 (2001).
[18]H. Xu, Q. Lu, Y. Li, W. Liu, X. Yi, Y. Wang, and M. Yue, "Reaction mechanism of Ca-reduction diffusion process used for sustainable recycling Nd–Fe–B sludge," J. Alloys Compd. **909**, 164744 (2022).
[19]X. B. Liu, Y. Ma, Z. Altounian, Q. Zhang, and J. Ping Liu, "First-principles survey on the doping of Ga in $Nd_2Fe_{14}B$," J. Appl. Phys. **115**(17), 17A702 (2014).
[20]V. Jagadeesha Angadi, K. M. Srinivasamurthy, M. Imran, S. P. Kubrin, M. Ubaidullah, S. F. Shaikh, H. Gao, H. Yang, V. K. Pattar, S. O. Manjunatha, and C. Prakash, Ceram. Int. **49**, 35213 (2023).

[21] Z. Lin, L. Zha, F. Wang, Z. Liu, R. Wu, J. Yang, M. Xue, W. Yang, G. Tian, X. Ma *et al.*, "Effect of Ce substitution on the structural and magnetic properties of $Nd_2Fe_{14}B$," Acta Mater. **200**, 502–509 (2020).
[22] J. Chaboy, C. Piquer, N. Plugaru, F. Bartolomé, M. A. Laguna-Marco, and F. Plazaola, "^{57}Fe Mössbauer and x-ray magnetic circular dichroism study of magnetic compensation of the rare-earth sublattice inNd_2–x$HoxFe_{14}B$ compounds," Phys. Rev. B **76**(13), 134408 (2007).
[23] O. Isnard and D. Fruchart, "Magnetism in Fe-based intermetallics: Relationships between local environments and local magnetic moments," J. Alloys Compd. **205**(1–2), 1–15 (1994).
[24] J. Wang, L. Liang, L. T. Zhang, M. Yano, K. Terashima, H. Kada, S. Kato, T. Kadono, S. Imada, T. Nakamura, and S. Hirano, "Mixed-valence state of Ce and its individual atomic moments in $Ce_2Fe_{14}B$ studied by soft x-ray magnetic circular dichroism," Intermetallics **69**, 42–46 (2016).
[25] M. Rosenberg, P. Deppe, M. Wójcik, and H. Stadelmeier, "A NMR and Mössbauer study of $Nd_2Fe_{14}B$," J. Appl. Phys. **57**(8), 4124–4126 (1985).
[26] C. Glorieux, J. Caerels, and J. Thoen, "Magnetic phase transition of gadolinium studied by acoustically detected magnetocaloric effect," J. Appl. Phys. **80**(6), 3412–3421 (1996).
[27] N. H. Duc, D. T. Kim Anh, and P. E. Brommer, "Metamagnetism, giant magnetoresistance and magnetocaloric effects in RCo_2-based compounds in the vicinity of the Curie temperature," Physica B **319**(1–4), 1–8 (2002).
[28] S. Bustingorry, F. Pomiro, G. Aurelio, and J. Curiale, "Second-order magnetic critical points at finite magnetic fields: Revisiting Arrott plots," Phys. Rev. B **93**(22), 224429 (2016).
[29] W. Dunhui, T. Shaolong, H. Songling, Z. Jianrong, and D. Youwei, "The magnetic phase transition and the low-field Arrott plots of $(GD_xDy_{1-x})Co_2$ compounds," J. Magn. Magn. Mater. **268**(1–2), 70–74 (2004).
[30] E. Belorizky, M. A. Fremy, J. P. Gavigan, D. Givord, and H. S. Li, "Evidence in rare-earth (R)–transition metal (M) intermetallics for a systematic dependence of R-M exchange interactions on the nature of the R atom," J. Appl. Phys. **61**(8), 3971–3973 (1987).
[31] See https://hpc.lzu.edu.cn/ for information about Lanzhou University Supercomputing Platform.